





COMMUNICATION

TMEM16A calcium-activated chloride currents in supporting cells of the mouse olfactory epithelium

Tiago Henriques^{1*}, Emilio Agostinelli^{1*}, Andres Hernandez-Clavijo¹, Devendra Kumar Maurya¹, Jason R. Rock², Brian D. Harfe³, Anna Menini¹, and Simone Pifferi¹

Glial-like supporting (or sustentacular) cells are important constituents of the olfactory epithelium that are involved in several physiological processes such as production of endocannabinoids, insulin, and ATP and regulation of the ionic composition of the mucus layer that covers the apical surface of the olfactory epithelium. Supporting cells express metabotropic P2Y purinergic receptors that generate ATP-induced Ca²⁺ signaling through the activation of a PLC-mediated cascade. Recently, we reported that a subpopulation of supporting cells expresses also the Ca²⁺-activated Cl⁻ channel TMEM16A. Here, we sought to extend our understanding of a possible physiological role of this channel in the olfactory system by asking whether Ca²⁺ can activate Cl⁻ currents mediated by TMEM16A. We use whole-cell patch-clamp analysis in slices of the olfactory epithelium to measure dose–response relations in the presence of various intracellular Ca²⁺ concentrations, ion selectivity, and blockage. We find that knockout of TMEM16A abolishes Ca²⁺-activated Cl⁻ currents, demonstrating that TMEM16A is essential for these currents in supporting cells. Also, by using extracellular ATP as physiological stimuli, we found that the stimulation of purinergic receptors activates a large TMEM16A-dependent Cl⁻ current, indicating a possible role of TMEM16A in ATP-mediated signaling. Altogether, our results establish that TMEM16A-mediated currents are functional in olfactory supporting cells and provide a foundation for future work investigating the precise physiological role of TMEM16A in the olfactory system.

Introduction

The olfactory epithelium is a pseudostratified epithelium composed of olfactory sensory neurons, glial-like supporting (or sustentacular) cells, basal cells, and microvillous cells, covered by a protective mucus layer composed of water, ions, and proteins secreted by Bowman's glands and supporting cells (Menco and Farbman, 1992; Menco et al., 1998). Although most studies concentrated on the physiological role of olfactory sensory neurons, as they detect odorant molecules, very few investigated how the supporting cells contribute to the epithelium homeostasis.

Supporting cells have columnar cell bodies that form a monolayer at the apical surface of the olfactory epithelium and basal processes extending to the basal lamina. The apical side of these cells bears several microvilli immersed in the mucus layer intermingling with cilia of olfactory sensory neurons. Supporting cells are electrically coupled by gap junctions composed at least by connexin 43 and 45, creating a syncytium for the diffusion of Ca²⁺ and other signaling molecules throughout the epithelium (Rash et al., 2005; Vogalis et al., 2005a,b).

These cells perform a large number of physiological functions. For example, they surround and provide structural support to olfactory sensory neurons, act as phagocytes of dead cells, and are involved in the metabolism of external compounds mediated by cytochrome P450 and other enzymes (Breipohl et al., 1974; Chen et al., 1992; Suzuki et al., 1996; Gu et al., 1998; Ling et al., 2004; Whitby-Logan et al., 2004). Neurotrophic and neuromodulator molecules such as endocannabinoids, insulin, and ATP are produced by supporting cells (Czesnik et al., 2007; Lacroix et al., 2008; Breunig et al., 2010; Hayoz et al., 2012). Moreover, they express metabotropic P2Y purinergic receptors, and stimulation with ATP induces Ca²⁺ signaling through the activation of a PLC-mediated cascade (Hegg et al., 2003, 2009; Gayle and Burnstock, 2005). Interestingly, several studies showed that ATP is involved in neuroprotection and neuroproliferation (Hassenklöver et al., 2009; Jia et al., 2009, 2010; Jia and Hegg, 2010). The mechanisms mediating the aforementioned functions are far from being completely elucidated.

¹Neurobiology Group, International School for Advanced Studies, Trieste, Italy; ²Center for Regenerative Medicine, Boston University School of Medicine, Boston, MA; ³Department of Molecular Genetics and Microbiology Genetics Institute, University of Florida, College of Medicine, Gainesville, FL.

*T. Henriques and E. Agostinelli contributed equally to this paper; Correspondence to Simone Pifferi: spifferi@sissa.it; D. Kumar Maurya's present address is Department of Molecular Biology, Umeå University, Umeå, Sweden.

© 2019 Henriques et al. This article is distributed under the terms of an Attribution–Noncommercial–Share Alike–No Mirror Sites license for the first six months after the publication date (see <http://www.rupress.org/terms/>). After six months it is available under a Creative Commons License (Attribution–Noncommercial–Share Alike 4.0 International license, as described at <https://creativecommons.org/licenses/by-nc-sa/4.0/>).

Moreover, supporting cells have peculiar electrical properties and express several channels involved in the regulation of the ionic composition of the mucus layer at the apical surface of the olfactory epithelium, contributing to the maintenance of a balance between salts and water. For example, the amiloride-sensitive Na^+ channel is highly expressed in microvilli of supporting cells (Menco et al., 1998), and it has been suggested that the cystic fibrosis transmembrane conductance regulator Cl^- channel and members of the aquaporin water channel family are possibly located in these cells, although their localization has not been conclusively demonstrated (Rochelle et al., 2000; Ablimit et al., 2006; Grubb et al., 2007; Lu et al., 2008; Merigo et al., 2011; Pfister et al., 2015).

We and others have recently shown that a relatively new discovered Ca^{2+} -activated Cl^- channel, TMEM16A, is expressed in olfactory supporting cells (Dauner et al., 2012; Maurya and Menini, 2014; Maurya et al., 2015). Interestingly, we found that TMEM16A expression is limited to supporting cells from a specific region of the olfactory epithelium (Maurya and Menini, 2014), although others, while confirming TMEM16A expression in the supporting cells, did not mention any zonal expression of the channel (Dauner et al., 2012). For this reason, here, we first tried to define whether a zonal expression of TMEM16A can be observed in the olfactory epithelium. By using immunohistochemistry on WT and TMEM16A knock out (KO) mice, we found that TMEM16A is expressed both in the ventral and dorsal zones of the olfactory epithelium, although its expression is higher in the region near the transition zone with the respiratory epithelium than in the dorsal zone.

Because TMEM16A is expressed in supporting cells, is it also mediating Ca^{2+} -activated Cl^- currents in these cells? To begin to address this question, we performed recordings in whole cells from mouse supporting cells after blocking gap junctions with 18β -glycyrrhetic acid (18β -GA; Davidson and Baumgarten, 1988) and recorded Ca^{2+} -activated Cl^- currents in WT but not TMEM16A KO mice, showing that TMEM16A is necessary for the activation of this current in mouse olfactory supporting cells. TMEM16A controls fluid secretion in airway and intestine epithelia (Rock et al., 2009; Benedetto et al., 2017, 2019), suggesting that TMEM16A could play a similar role in supporting cells. Moreover, TMEM16A can modulate several aspects of Ca^{2+} homeostasis, consequently regulating different signaling cascades (Kunzelmann et al., 2016; Cabrita et al., 2017). What signaling pathway leads to the activation of TMEM16A-mediated currents in supporting cells? We found that stimulation of purinergic receptors with ATP activated a TMEM16A-dependent current.

In summary, TMEM16A can produce Ca^{2+} -activated Cl^- currents in response to extracellular ATP in olfactory supporting cells. Finally, we picture and discuss the different scenarios of physiological functions of supporting cells and their chloride conductance.

Materials and methods

Animals

Mice were handled in accordance with the guidelines of the Italian Animal Welfare Act and European Union guidelines on

animal research under a protocol approved by the ethics committee of the International School for Advanced Studies. Postnatal days 0–4 (P0–P4) mice were decapitated before nose removal. Experiments were performed on tissues from C57BL/6 mice or from TMEM16A WT and TMEM16A KO littermate mice obtained by breeding heterozygous mice generated by Rock et al. (2008).

Immunohistochemistry

Coronal sections of the olfactory epithelium and immunohistochemistry were obtained as previously described (Maurya and Menini, 2014; Maurya et al., 2015). Briefly, the dissected nose was fixed in 4% paraformaldehyde PBS for 4 h at 4°C. Tissues were equilibrated overnight at 4°C in 30% (wt/vol) sucrose and then embedded in optimal cutting temperature compound (Bio-optica) and stored at -80°C . Coronal sections 12- to 14- μm thick were cut with a cryostat. Before using primary antibodies, sections were incubated in blocking solution (2% FBS [vol/vol] and 0.2% [vol/vol] Triton X-100 in PBS) for 90 min. Then, they were incubated with the primary antibody (diluted in the blocking solution) overnight at 4°C. The following primary antibodies (catalog number, dilution; company) were used: polyclonal goat anti-OMP (544–10001, 1:1,000; Wako Chemicals), mouse monoclonal acetylated tubulin (T7451, 1:100; Sigma), and rabbit polyclonal anti-TMEM16A (ab53212, 1:50; Abcam). Sections were then rinsed with 0.1% (vol/vol) Tween 20 in PBS (PBS-T) and incubated with the fluorophore-conjugated secondary antibody (diluted in PBS-T) for 2 h at room temperature. The following secondary antibodies were used: donkey anti-rabbit Alexa Fluor 488 (A-21206; Life Technologies), donkey anti-goat Alexa Fluor 594 (A-11058; Life Technologies), and donkey anti-mouse Alexa Fluor 594 (A-21203; Life Technologies). After washing with PBS-T, sections were treated with 0.1 $\mu\text{g}/\text{ml}$ DAPI for 30 min, washed with PBS-T, and mounted with Vectashield (Vector Laboratories).

Immunoreactivity was visualized with a confocal microscope (TCS SP2; Leica). Images were acquired using Leica software (at $1,024 \times 1,024$ -pixel resolution) and were not modified other than to balance brightness and contrast, unless otherwise specified. Nuclei were stained by DAPI. Control experiments without the primary antibodies gave no signal. In addition, negative control experiments for the localization of TMEM16A were performed in tissues from TMEM16A KO mice following the same protocol used in WT mice.

Preparation of acute slices of the olfactory epithelium

Acute coronal slices of the olfactory epithelium of P0–P4 mice were prepared with slight modifications of the methods previously described to obtain slices of the vomeronasal organ (Shimazaki et al., 2006; Dibattista et al., 2008; Pietra et al., 2016; Wong et al., 2018). P0–P4 mice are suitable for this study, because TMEM16A is already expressed in the olfactory epithelium at this age (Maurya and Menini, 2014; Maurya et al., 2015). The nose of a P0–P4 mouse was dissected en bloc and embedded in 3% Type I-A agarose prepared in artificial cerebrospinal fluid (ACSF) once the solution cooled to 38°C . ACSF contained (in mM) 120 NaCl, 25 NaHCO_3 , 5 KCl, 1 MgSO_4 , 1 CaCl_2 , 10 HEPES, and 10 glucose, pH 7.4, with NaOH. Coronal slices of 300- μm

thickness were cut with a vibratome (Vibratome 1000 Plus Sectioning System) and kept in cold oxygenated ACSF until use.

Whole-cell recordings from supporting cells of the olfactory epithelium

Slices were transferred to a recording chamber continuously perfused with oxygenated ACSF. Slices were viewed with an upright microscope (BX51WI; Olympus) equipped with infrared differential contrast optics, a camera (DFK 72BUC02; Imaging Source) and a 40× water-immersion objective with an additional 2× auxiliary lens. Extracellular solutions were exchanged or stimuli were delivered through an eight-in-one multibarrel perfusion pencil connected to a ValveLink8.2 pinch valve perfusion system (Automate Scientific).

Supporting cells were identified by their morphology, and whole-cell experiments were obtained by patching the apical part of supporting cells. Fluorescein (10 μg/ml) dissolved in the pipette solution diffused into the cell and allowed visualization under blue light of the fluorescence image of the cell (Fig. 2 A). Patch pipettes were pulled from borosilicate capillaries (WPI) with a Narishige PC-10 puller and had resistances of 3–5 MΩ when filled with intracellular solution. Electrophysiological recordings were obtained using a MultiClamp 700B amplifier controlled by Clampex 10.6 via a Digidata 1550B (Molecular Devices). Data were low-pass filtered at 2 kHz and sampled at 10 kHz. Experiments were performed at room temperature (20–25°C).

The extracellular Ringer's solution contained (in mM) 140 NaCl, 5 KCl, 2 CaCl₂, 1 MgCl₂, 10 HEPES, and 10 glucose, pH 7.4. For ionic selectivity experiments, NaCl in the extracellular Ringer's solution was omitted and 250 mM sucrose was added to maintain the osmolarity (sucrose Ringer's) or NaCl was replaced with equimolar NMDG-Cl (NMDG Ringer's). We used various intracellular solutions filling the patch pipette according to the type of experiment. For recordings of voltage-gated currents, the pipette solution contained (in mM): 145 KCl, 4 MgCl₂, 11 EGTA, and 10 HEPES, adjusted to pH 7.2 with KOH. For recordings of Ca²⁺-activated currents, the intracellular solutions contained (in mM) 140 CsCl, 10 HEDTA, and 10 HEPES adjusted to pH 7.2 with CsOH, and no added Ca²⁺ for the nominally 0 Ca²⁺ solution or various added Ca²⁺ concentrations, as calculated with the program WinMAXC (C. Patton, Stanford University, Stanford, CA), to obtain free Ca²⁺ in the range between 0.5 and 3.8 μM (Patton et al., 2004). 10 mM HEDTA had the best buffer efficacy in the desired range of free Ca²⁺ concentrations. We added 1.242, 3.209, or 5.806 mM CaCl₂ to obtain 0.5, 1.5, or 3.8 μM free Ca²⁺, respectively, as described previously (Pifferi et al., 2006, 2009; Cenedese et al., 2012; Betto et al., 2014; Amjad et al., 2015). The free Ca²⁺ concentrations were also experimentally determined by Fura-4F (Thermo Fisher Scientific) measurements by using an LS-50B luminescence spectrophotometer (PerkinElmer).

For recordings of ATP-activated currents, the pipette solution contained (in mM) 140 CsCl, 2 HEDTA, and 10 HEPES, adjusted to pH 7.2 with CsOH. I-V relations were measured using a ramp protocol from -80 mV to +80 mV at 0.16 mV/ms.

The bath was grounded via a 3 M KCl agar bridge connected to an Ag/AgCl reference electrode. Liquid junction potentials

were calculated using pClamp 10.6 (based on Barry, 1994), and the applied voltages were corrected offline for the following values (in mV) in the indicated bathing solutions: -4.7 in Ringer's solution, +7.9 in sucrose Ringer's solution, and -5.7 in NMDG Ringer's solution.

The following chemicals were prepared as stock solutions as indicated and diluted to the final concentration in the bathing solution on the day of the experiment: 100 mM 18β-GA in ethanol, 30 mM ATP in Ringer's solution, stored at -20°C; and 1 mM Ani9 in DMSO, stored at +4°C. The final concentration of 18β-GA was 20 μM as previously used by Vogalis et al. (2005a,b) to substantially reduce the resting leak conductance in olfactory supporting cells. At this concentration, 18β-GA is reported to block most of the gap-junction-mediated current in fibroblasts (Davidson and Baumgarten, 1988). The final concentration of ATP was 30 μM, which is slightly higher than the concentration of 10 μM used by Hegg et al. (2003) to activate P2Y receptors expressed in supporting cells and induce an intracellular Ca²⁺ increase. All chemicals were purchased from Sigma unless otherwise specified.

Confocal Ca²⁺ imaging

Slices were loaded with 20 μM Cal-520AM (Santa Cruz Biotechnologies) for 90 min at room temperature in ACSF. The concentration of Cal-520AM required for cell loading in our slices was determined empirically after testing several dye working solutions from 10 to 20 μM, as suggested by the technical information sheet. To help dye uptake, Pluronic F-127 was added at final concentration of 0.2 mg/ml. After washing, the slices were kept in ACSF solution until use. Stock solution of Cal-520AM was prepared in DMSO at 2 mM and stored at -20°C. Pluronic F-127 was weekly dissolved in DMSO at 200 mg/ml concentration. A gravity-driven multivalve perfusion system (Automate Scientific) was used to deliver the stimuli.

An inverted Nikon AIR confocal microscope was used for data acquisition with a 60× oil-immersion objective (numerical aperture 1.3) using NIS Element software (Nikon). Cal-520 fluorescence was excited using a krypton-argon ion laser. To reduce dye bleaching and photodamage, only 1–4% of the laser power and a resonance scanning mirror was used. Fluorescence emission between 500 and 600 nm was captured using a variable band pass system. Data were recorded after averaging eight frames to get a final acquisition frequency of 0.23 Hz with 1,024 × 512-pixel resolution. Recordings were obtained 50–100 μm below the slice surface to avoid damaged cells.

Changes in fluorescence were measured in regions of interest drawn around a single supporting cell using ImageJ 1.51s (National Institutes of Health). Data are presented as normalized fluorescence changes, $\Delta F/F_0 = (F(t) - F_0)/F_0$, where F_0 is the average of fluorescence intensity before the application of the first stimulus and $F(t)$ is the fluorescence amplitude at time t . Further analysis and figures were made with IgorPro 6.3.7.2 (WaveMetrics). In some experiments, the reduction of fluorescence signal due to photobleaching was mathematically corrected using the exponential decay observed in nonresponding cells (Thomas et al., 2000). We considered a cell responsive if (a) there was no spontaneous activity; (b) after stimulation, $\Delta F/F_0$

was higher than the average of the prestimulus (10-s time window) plus three SDs for at least 3 s; and (c) there was no response to ACSF solution application.

Analysis of electrophysiological data

IGOR Pro software (WaveMetrics) was used for data analysis and to produce the figures. All averaged data from individual experiments in different cells are presented as mean \pm SEM and number of cells (*n*). Cells were obtained from at least three different WT or KO mice. In the box plot, horizontal lines represent the median, upper and lower box boundaries represent the 25th and 75th percentile, and upper and lower whiskers represent the 10th and 90th percentiles. Statistical analyses of normally distributed data (Jarque-Bera test) were performed using a *t* test, one-sample *t* test, or one-way ANOVA with Tukey test. For not normally distributed data, the Wilcoxon-Mann-Whitney *U* test and Kruskal-Wallis with Dunn-Holland-Wolfe test were used. *P* values of <0.05 were considered statistically significant.

Results

TMEM16A expression in olfactory supporting cells

Considering that the physiological role of TMEM16A in olfactory supporting cells is unknown, we started studying the TMEM16A expression in the olfactory epithelium. We previously reported a not-uniform immunoreactivity for TMEM16A in the olfactory epithelium of postnatal mice (Maurya and Menini, 2014). Indeed, we found that TMEM16A is expressed only in the supporting cells in the ventral region of olfactory epithelium close to the respiratory epithelium. However, Dauner et al. (2012) did not show this specific localization and instead found TMEM16A in supporting cells from all olfactory epithelium. For this reason, we first asked whether TMEM16A is specifically expressed only near the transition zone, and therefore has a physiological role only in that zone, or if it is also poorly expressed in other regions of the olfactory epithelium.

By immunohistochemistry, we confirmed previous results that TMEM16A is strongly expressed at the apical surface of the ventral region of the olfactory epithelium near the transition zone with the respiratory epithelium, but we also identified a weak staining for TMEM16A in the dorsal zone that could be revealed only by digital enhancement of the signal intensity (Fig. 1, A-D). We performed control experiments in the olfactory epithelium of TMEM16A KO mice following the same protocol and found no signal for TMEM16A, confirming the specificity of the immunostaining obtained in WT mice (Fig. 1, C and D). To visualize olfactory neurons, we used the olfactory marker protein, a typical marker for mature olfactory sensory neurons (Keller and Margolis, 1975), while the cilia of olfactory neurons were identified with acetylated tubulin, a canonical marker for cilia (Piperno and Fuller, 1985). In both the transition and dorsal zones, TMEM16A was expressed at the apical surface of the olfactory epithelium of WT mice, and it did not overlap with the upper layer stained by acetylated tubulin, confirming that TMEM16A was not expressed in olfactory sensory neurons but was localized at the apical portion of supporting cells.

These results confirm and extend previous data showing that TMEM16A is highly expressed in the transition zone (Fig. 1 C), while it is poorly expressed in the dorsal zone (Fig. 1 D).

Ca²⁺-activated Cl⁻ currents in supporting cells of the mouse olfactory epithelium

TMEM16A is a Ca²⁺-activated Cl⁻ channel, but currents caused by the activity of this channel have not yet been reported in olfactory supporting cells. Therefore, we performed electrophysiological experiments to investigate the presence of functional Ca²⁺-activated Cl⁻ channels in these cells.

First, we established the viability of obtaining electrophysiological recordings from supporting cells by measuring basic electrophysiological properties and voltage-gated currents. Whole-cell recordings were obtained from supporting cells at the apical surface of neonatal mouse olfactory epithelium slices. To visually identify cells, fluorescein was included in the intracellular solution filling the patch pipette and diffused inside the cell after rupturing the membrane to obtain the whole-cell configuration. The fluorescence image in Fig. 2 A reveals the typical morphology of a supporting cell, with the cell body located in the apical region and processes extending toward the basal part of the epithelium. In this study, we only analyzed recordings from supporting cells clearly identified by their morphology. Passive membrane properties in the presence of KCl in the pipette had the following values: mean resting potential, -41 ± 1 mV (*n* = 18); input resistance, 261 ± 88 M Ω (*n* = 11); and capacitance, 17 ± 1 pF (*n* = 17). Next, we investigated the presence of voltage-gated currents (Fig. 2). As supporting cells have very large leak currents (see Fig. 2, D and E), voltage-gated currents could only be revealed after subtraction of the leak currents using the P/4 protocol (Fig. 2 B). Voltage steps more positive than approximately -60 mV elicited transient inward currents followed by outward currents. Average I-V relations measured at the peak of the inward currents or at the end of the sustained outward currents (Fig. 2 C) are largely similar to those previously reported by Vogalis et al. (2005a), who showed that inward and outward currents were mainly due to voltage-gated Na⁺ and K⁺ channels. Our results confirm the viability of electrophysiological recordings of supporting cells in our slice preparation.

Before measuring Ca²⁺-activated currents, we tested whether we could block the large leak conductance measured in the presence of nominally 0 Ca²⁺. Indeed, in extracellular Ringer's solution, the average current was -687 ± 206 pA at -80 mV and $3,678 \pm 1,065$ pA at $+80$ mV (*n* = 4), with an intracellular solution containing CsCl (Fig. 2, D and E). After pretreatment of slices for ~ 1 h with $20 \mu\text{M}$ 18 β -GA, a gap junction blocker, currents were significantly reduced to -174 ± 18 pA at -80 mV and 459 ± 54 pA at $+80$ mV (*n* = 17, *P* < 0.001, unpaired Wilcoxon-Mann-Whitney *U* test; Fig. 2, D and E), confirming that $20 \mu\text{M}$ 18 β -GA partially blocks the leak currents as previously reported (Vogalis et al., 2005a,b). Thus, all the subsequent experiments were performed with intracellular CsCl after pretreatment with $20 \mu\text{M}$ 18 β -GA.

To establish whether a current could be activated by Ca²⁺ in supporting cells, we compared currents measured with intracellular solutions containing various Ca²⁺ concentrations

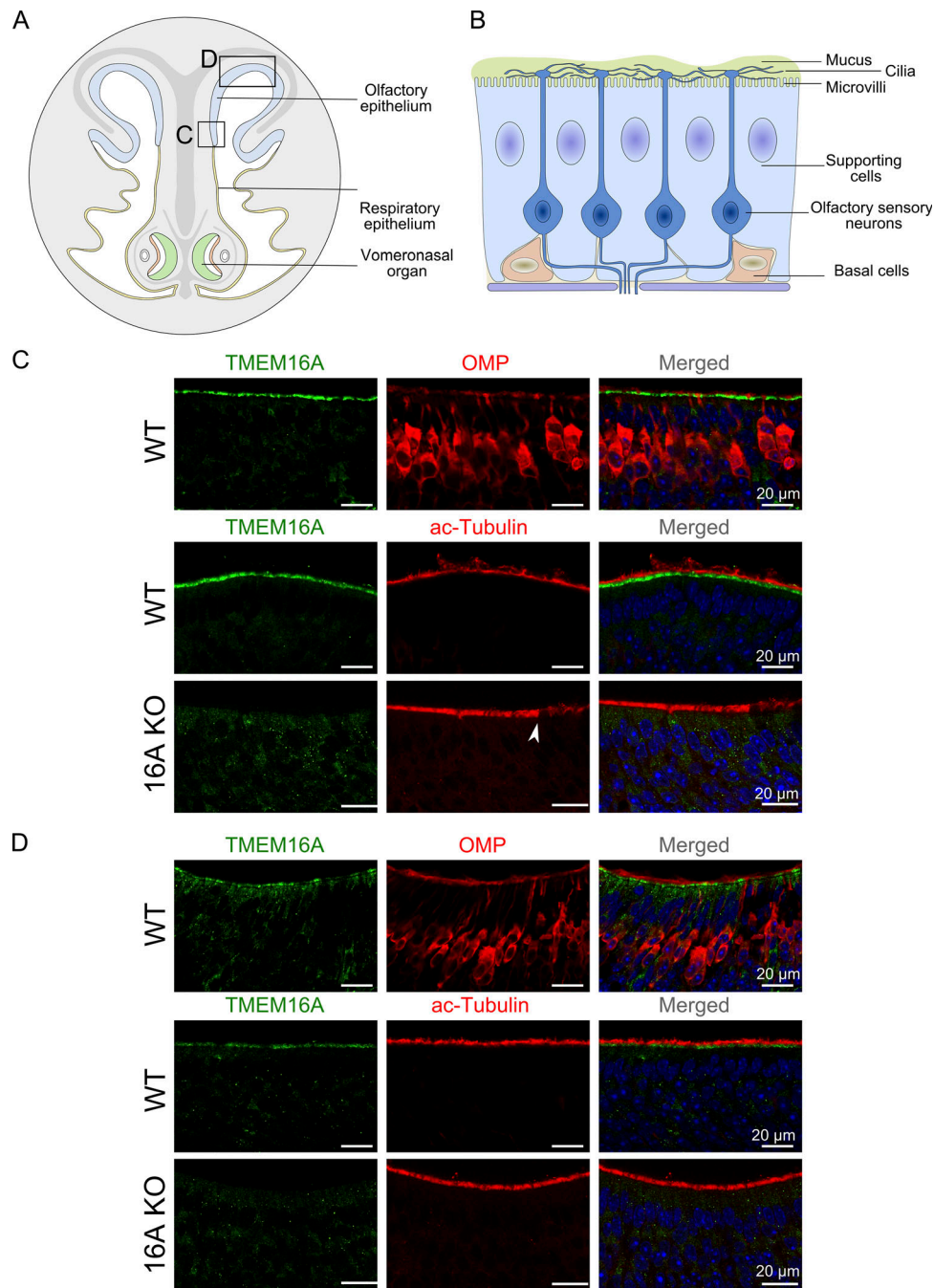


Figure 1. **TMEM16A expression in the olfactory epithelium.** (A) Schematic drawing of a nose coronal section showing the olfactory epithelium, respiratory epithelium, and vomeronasal organ. (B) The olfactory epithelium is composed of supporting cells, olfactory sensory neurons, and basal cells. (C and D) Confocal micrographs of coronal sections of the olfactory epithelium from an area near the transition zone with the respiratory epithelium (C) or from the dorsal zone (D). The signal intensity in D was digitally enhanced to reveal a weak staining for TMEM16A. No immunoreactivity to TMEM16A was detectable at the apical surface of the olfactory epithelium in TMEM16A KO mice (C and D). Arrowhead in C indicates the transition from the olfactory to respiratory epithelium. Cell nuclei were stained by DAPI. OMP, olfactory marker protein.

ranging from nominally 0 to 3.8 μM Ca^{2+} . Since we have previously shown that cells in the transition zone display a strong immunoreactivity for the Ca^{2+} -activated Cl^- channel TMEM16A (Fig. 1 C), we first recorded from supporting cells located in this area.

Fig. 3 A shows currents in the presence of increasing $[\text{Ca}^{2+}]_i$. The activation of the current by voltage steps in the presence of

0.5 and 1.5 μM Ca^{2+} was time dependent, with an instantaneous component followed by relaxation (Fig. 3 A, red and blue traces). Indeed, at +80 mV, the instantaneous outward current was followed by a small additional outward relaxation, while at -80 mV, the instantaneous inward current was followed by a more pronounced relaxation toward less negative values. Moreover, when the voltage was stepped to -80 mV at the end of the

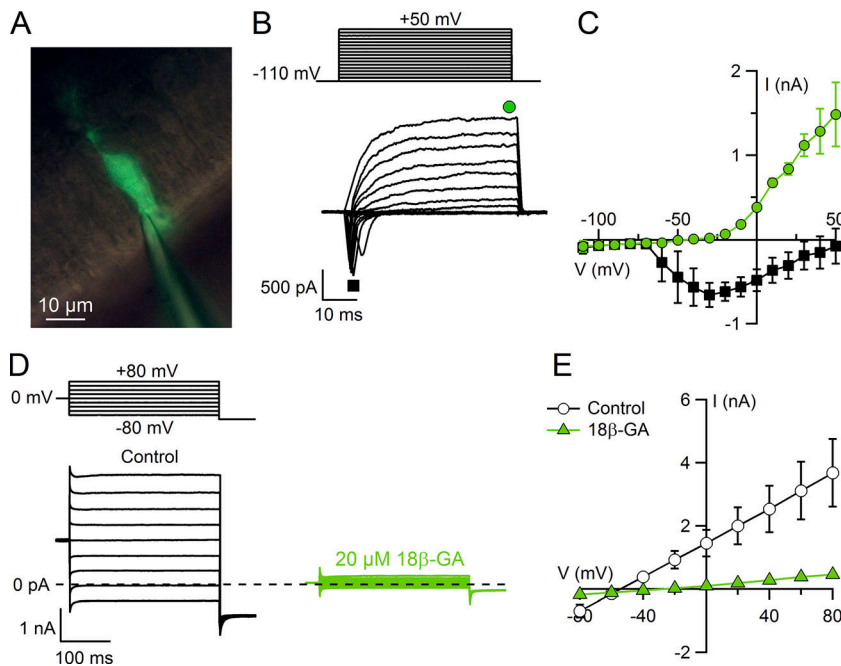


Figure 2. Voltage-gated currents and leak currents in olfactory supporting cells. (A) Fluorescence micrograph of a supporting cell filled with fluorescein through the patch pipette. (B) Representative whole-cell currents recorded using the voltage protocol indicated at the top of the panel. The holding potential was -110 mV, and voltage steps in 10 -mV increments were applied up to $+50$ mV. Leak currents were subtracted using the P/4 protocol. (C) Plot of average \pm SEM amplitudes of inward (black squares) and outward (green circles) currents versus the test potential ($n = 3$). (D) Representative whole-cell currents recorded from two different supporting cells in control condition (black traces) and after preincubation with $20 \mu\text{M}$ $18\beta\text{-GA}$ (green traces). The holding potential was 0 mV, and voltage steps from -80 mV to $+80$ mV with 20 -mV increments were applied as indicated at the top of the panel. (E) Plot of average \pm SEM current amplitudes measured at the end of voltage pulses versus the test potential from cells in control condition (white circles; $n = 4$) and after preincubation with $20 \mu\text{M}$ $18\beta\text{-GA}$ (green triangles; $n = 17$).

protocol, deactivating inward tail currents were observed. I-V relations measured at the end of voltage pulses showed an outward rectification at $0.5 \mu\text{M}$ Ca^{2+} that became less pronounced as $[\text{Ca}^{2+}]_i$ increased (Fig. 3, A and B). The rectification index, calculated as the ratio between the current at $+80$ and -80 mV, decreased from 4.1 ± 0.3 ($n = 5$) at $0.5 \mu\text{M}$ Ca^{2+} to 1.24 ± 0.06 ($n = 7$) at $3.8 \mu\text{M}$ (Fig. 3 C; $P < 0.001$, Dunn-Holland-Wolfe test).

Dose-response relations were evaluated at $+80$ and -80 mV. The average current at $+80$ mV in the presence of nominally 0 Ca^{2+} (residual leak current, I_L) was 459 ± 54 pA ($n = 17$), while $0.5 \mu\text{M}$ Ca^{2+} elicited comparatively larger currents ($1,151 \pm 192$ pA, $n = 5$). Further increases of $[\text{Ca}^{2+}]_i$ produced currents of higher amplitudes, reaching an average of $2,268 \pm 137$ pA ($n = 33$) with $1.5 \mu\text{M}$ Ca^{2+} and $2,328 \pm 296$ pA ($n = 7$) with $3.8 \mu\text{M}$ Ca^{2+} (Fig. 3 D). The average current amplitudes were plotted versus $[\text{Ca}^{2+}]_i$ and fit at each voltage by the Hill equation:

$$I = I_L + (I_{\max} - I_L) [\text{Ca}^{2+}]_i^{n_H} / ([\text{Ca}^{2+}]_i^{n_H} + K_{1/2}^{n_H}), \quad (1)$$

where I is the current, I_L is the residual leak current in the presence of nominally 0 Ca^{2+} , I_{\max} is the maximal current, $K_{1/2}$ is the half-maximal $[\text{Ca}^{2+}]_i$, and n_H is the Hill coefficient. The Hill coefficient had the same value of 2.5 at both voltages, while $K_{1/2}$ decreased with membrane depolarization from $1.5 \mu\text{M}$ at -80 mV to $0.6 \mu\text{M}$ at $+80$ mV (Fig. 3 D), indicating that the Ca^{2+} sensitivity is slightly voltage dependent.

The ionic selectivity was evaluated by replacing NaCl in the extracellular Ringer's solution with sucrose or NMDG-Cl (Fig. 3, E-H). In the presence of low extracellular Cl^- , the reversal potential of the Ca^{2+} -activated current shifted toward positive values, as expected for Cl^- -selective channels in our ionic conditions, with an average shift of reversal potential of 40 ± 4 mV ($n = 7$). When NaCl was replaced with NMDG-Cl, a very small shift of the reversal potential of 4.2 ± 0.2 mV ($n = 4$) was measured, confirming the Cl^- selectivity of these channels.

Altogether, the time dependence of current activation by voltage, change of rectification of the I-V relation depending on $[\text{Ca}^{2+}]_i$, voltage dependence of Ca^{2+} sensitivity, and Cl^- selectivity are typical hallmarks of Ca^{2+} -activated Cl^- channels (Huang et al., 2012; Pedemonte and Galletta, 2014), suggesting that these channels may be responsible for the measured currents.

As we have shown that a weak immunoreactivity for TMEM16A was also present in supporting cells from the dorsal zone of the olfactory epithelium (Fig. 1 D), we also performed electrophysiological recordings in this zone (Fig. 4). The typical features of Ca^{2+} -activated Cl^- currents were present in several cells (represented by colored traces; Fig. 4, A and B) but absent in other cells (gray traces). We estimated that in the presence of $1.5 \mu\text{M}$ Ca^{2+} , $\sim 65\%$ of the measured supporting cells (16 out of 24) from the dorsal zone had a Ca^{2+} -activated current, although its amplitude was significantly smaller than that measured in cells from the transition zone (Fig. 4 C; Tukey test after one way ANOVA), confirming the lower expression of TMEM16A observed in immunohistochemistry.

Furthermore, the fit of dose-response relations measured in the dorsal zone yielded Hill coefficient values of 2.8 at -80 mV and 2.7 at $+80$ mV, while $K_{1/2}$ decreased with membrane depolarization from $1.2 \mu\text{M}$ at -80 mV to $0.7 \mu\text{M}$ at $+80$ mV (Fig. 4 D), similar to values obtained from supporting cells in the transition zone. The average shift of reversal potential upon reduction of extracellular Cl^- by replacement of NaCl with sucrose was $+41 \pm 4$ mV ($n = 6$), indicating a higher permeability for Cl^- than for Na^+ (Fig. 4, E and F).

Altogether, these results indicate that although the dorsal zone has on average a lower Ca^{2+} -activated Cl^- current compared with the transition zone, the biophysical properties of the channels are the same.

To measure the extracellular pharmacological block of Ca^{2+} -activated Cl^- currents, we tested Ani9, a recently identified

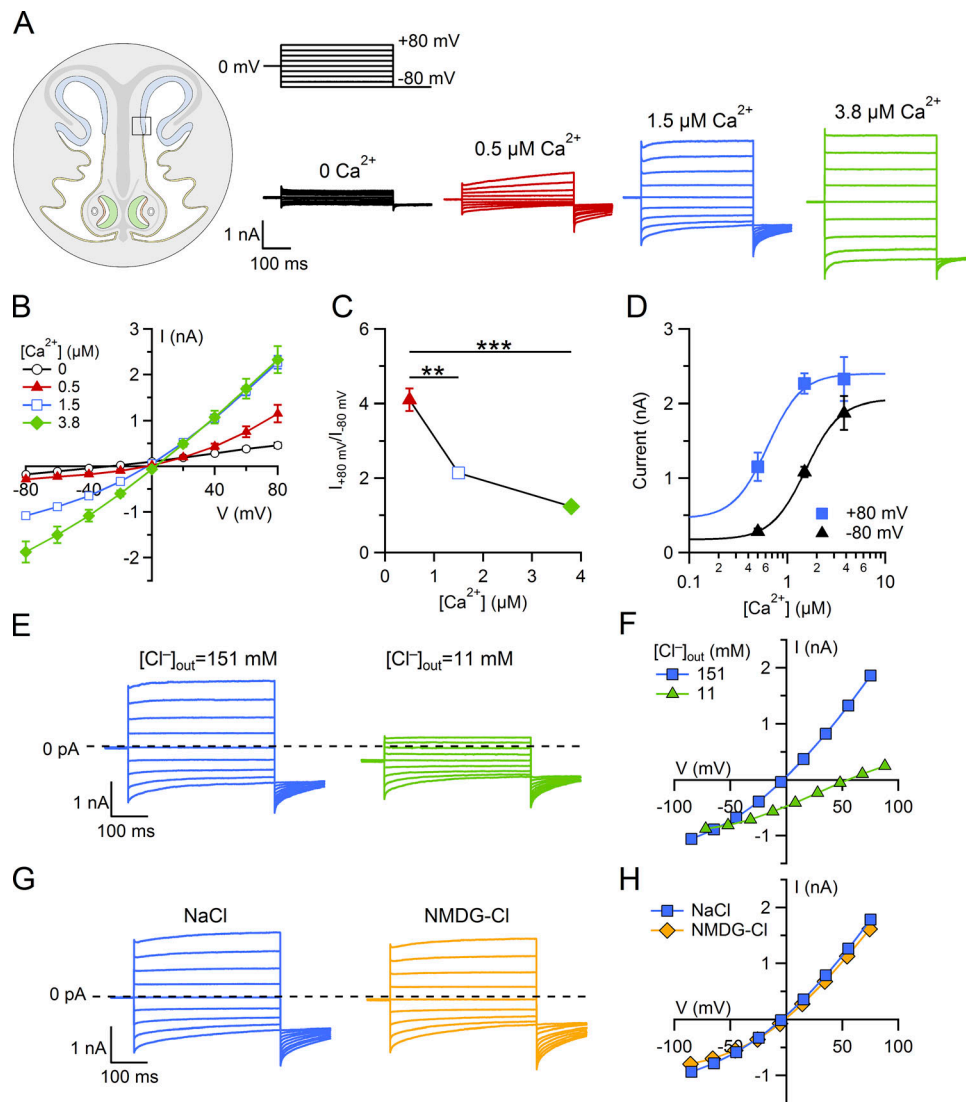


Figure 3. Ca^{2+} -activated Cl^- currents in supporting cells from a region of the olfactory epithelium near the transition zone with the respiratory epithelium. (A) Representative whole-cell currents recorded from different supporting cells with pipette solutions containing the indicated $[\text{Ca}^{2+}]_i$. The holding potential was 0 mV, and voltage steps from -80 mV to $+80$ mV with 20-mV increments, followed by a step to -80 mV, were applied as indicated at the top of the panel. (B) Average \pm SEM of steady-state I-V relations in the presence of the following $[\text{Ca}^{2+}]_i$: nominally 0 ($n = 17$), $0.5 \mu\text{M}$ ($n = 5$), $1.5 \mu\text{M}$ ($n = 33$), and $3.8 \mu\text{M}$ ($n = 7$). (C) Average \pm SEM of ratios between the currents measured at $+80$ and -80 mV at different $[\text{Ca}^{2+}]_i$ from the same experiments shown in B (**, $P < 0.01$; ***, $P < 0.001$, Dunn-Holland-Wolfe test after Kruskal-Wallis test). (D) Comparison of dose-responses at $+80$ and -80 mV, from the same experiments shown in B, fitted to the Hill equation (Eq. 1). The error bars indicate SEM. (E and F) Representative whole-cell currents recorded with pipette solution containing $1.5 \mu\text{M}$ Ca^{2+} . (E and G) Extracellular ion concentrations were modified by replacing 140 mM NaCl in the Ringer's solution with sucrose, reducing the extracellular $[\text{Cl}^-]$ to the indicated concentrations (E) or with NMDG-Cl (G). (F-H) Current amplitudes measured at the end of voltage pulses versus the test potential from the cells shown respectively in E-G.

potent selective blocker for TMEM16A (Seo et al., 2016). Indeed, it has been shown that $1 \mu\text{M}$ Ani9 does not significantly affect TMEM16B channel activity while it almost completely blocks TMEM16A-mediated currents (Seo et al., 2016). Fig. 5 (A-C) shows that $1 \mu\text{M}$ Ani9 reduced current amplitudes activated by $1.5 \mu\text{M}$ Ca^{2+} of $62 \pm 3\%$ at $+80$ mV and $61 \pm 3\%$ at -80 mV ($n = 10$, $P < 0.001$, one-sample t test), inducing a significant block of the current. The blockage by Ani9 supports the hypothesis that TMEM16A mediates the measured Ca^{2+} -activated Cl^- currents.

To determine the contribution of TMEM16A to Ca^{2+} -activated Cl^- currents in supporting cells, we compared currents from WT

and TMEM16A KO mice (Rock et al., 2008). Fig. 6 A shows the comparison between representative recordings from supporting cells from WT (black and blue traces) or TMEM16A KO (orange and red traces) mice. Current amplitudes in the presence of $1.5 \mu\text{M}$ Ca^{2+} from TMEM16A KO mice (red) were not significantly different from currents measured in the absence of Ca^{2+} (orange; $P > 0.05$, Tukey test after one-way ANOVA; Fig. 6 B), showing the absence of Ca^{2+} -activated currents in TMEM16A KO mice. The same experiments were performed also in supporting cells in the dorsal zone and yielded similar results. These data demonstrate that TMEM16A is a necessary component of the

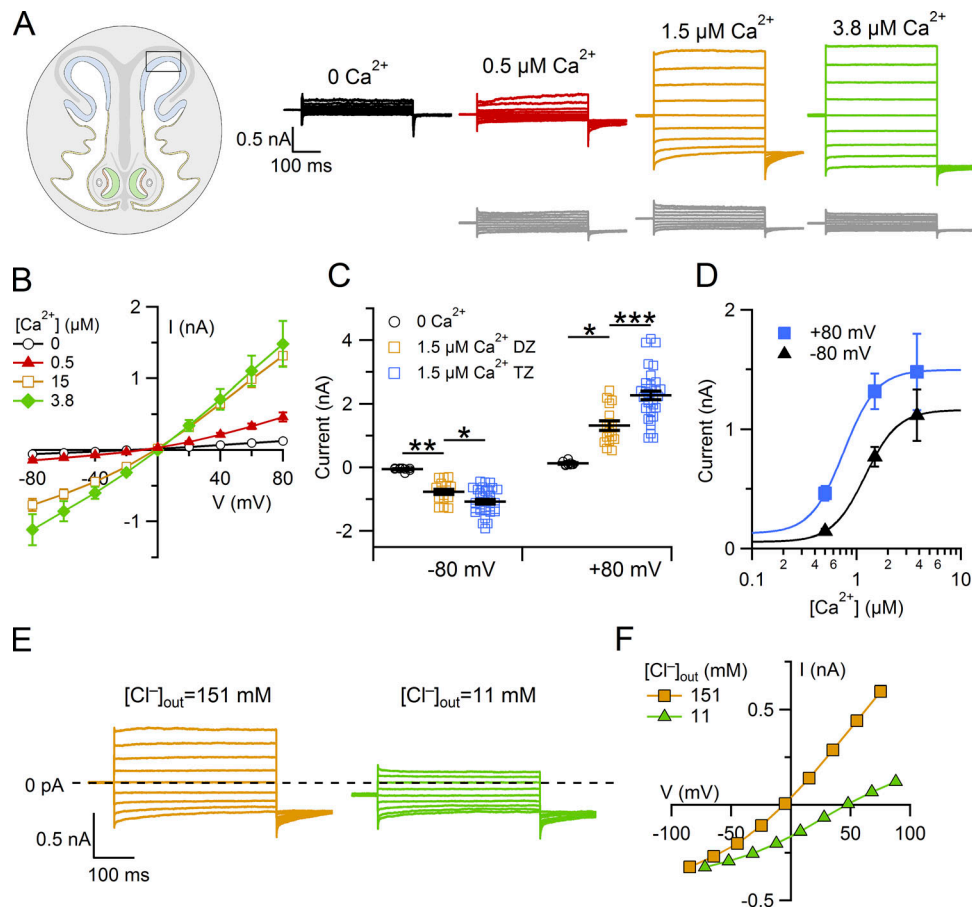


Figure 4. **Ca²⁺-activated chloride current in supporting cells from the dorsal zone of the olfactory epithelium.** (A) Representative whole-cell currents recorded from different supporting cells from the dorsal zone with pipette solutions containing the indicated [Ca²⁺]. The holding potential was 0 mV, and voltage steps from -80 mV to +80 mV with 20-mV increments, followed by a step to -80 mV, were applied as shown in the top panel of Fig. 3 A. (B) Average ± SEM of steady-state I-V relations in the presence of the following [Ca²⁺]: nominally 0 (*n* = 9), 0.5 μM (*n* = 9), 1.5 μM (*n* = 16), and 3.8 μM (*n* = 4). (C) Scatter dot plot with average ± SEM showing current amplitudes measured at -80 and +80 mV with the indicated [Ca²⁺]_i in the dorsal zone (DZ) or transition zone (TZ). Number of cells indicated in the legends of Fig. 3 B or 4 B for the TZ or DZ, respectively. *, *P* < 0.05; **, *P* < 0.01; ***, *P* < 0.001; Tukey test after one way ANOVA. (D) Comparison of dose-responses at +80 and -80 mV, from the same experiments shown in B, fitted to the Hill equation (Eq. 1). The error bars indicate SEM. (E) Representative whole-cell currents recorded with pipette solution containing 1.5 μM Ca²⁺. Extracellular ion concentrations were modified by replacing 140 mM NaCl in the Ringer's solution with sucrose, reducing the extracellular [Cl⁻] to the indicated concentrations. (F) Current amplitudes measured at the end of voltage pulses versus the test potential from the cell shown in E.

Ca²⁺-activated Cl⁻ currents in supporting cells of the olfactory epithelium.

ATP activates TMEM16A-dependent currents in supporting cells

As extracellular ATP elicits a transient increase in intracellular Ca²⁺ through activation of G-protein-coupled P2Y receptors and Ca²⁺ release from intracellular stores in olfactory supporting cells (Czesnik et al., 2006; Hassenklöver et al., 2008; Hegg et al., 2009), we hypothesized that ATP stimulation could activate a Ca²⁺-activated Cl⁻ current in these cells. Therefore, we first used confocal Ca²⁺ imaging to determine if ATP could elicit an increase in intracellular Ca²⁺ in our experimental conditions. Fig. 7 (A and B) shows that 30 μM ATP induced a significant transient increase of the intracellular Ca²⁺ concentration that returned to baseline level after several seconds in three selected supporting cells. Recordings from several slices showed that 95% of the supporting cells (80 of 84 cells from four slices)

responded to ATP stimulation with a transient increase of intracellular Ca²⁺.

Next, we used whole-cell recordings to test whether the Ca²⁺ increase induced by ATP stimulation could activate Ca²⁺-activated Cl⁻ channels in supporting cells. We lowered the intracellular concentration of HEDTA from 10 to 2 mM to reduce Ca²⁺ buffering that could decrease the intracellular Ca²⁺ increase. 30 μM ATP at the holding potential of -80 mV induced large inward currents that slowly recovered to baseline (Fig. 8 A, black trace). The I-V relation measured close to the peak of the response to ATP (Fig. 8 B, indicated as b) showed an outward rectification, resembling the outward rectification of the Ca²⁺-activated Cl⁻ current measured in the presence of 1.5 μM Ca²⁺ (Fig. 3 B).

To determine the contribution of TMEM16A to the ATP-induced current, we recorded responses to ATP in supporting cells from TMEM16A KO mice (Fig. 8 A, orange trace). Our experiments show that the average peak inward current induced

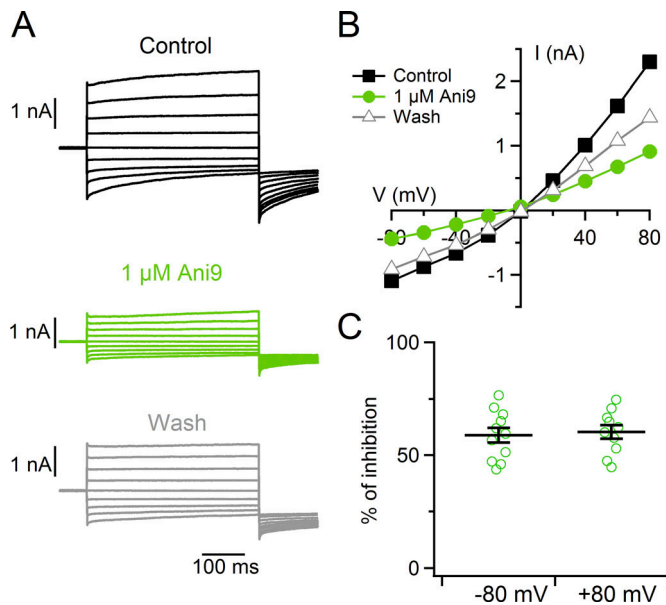


Figure 5. Ca^{2+} -activated currents in supporting cells are blocked by the TMEM16A inhibitor Ani9. (A) Representative whole-cell recordings obtained with an intracellular solution containing $1.5 \mu\text{M Ca}^{2+}$ (voltage protocol as in Fig. 3 A). The cell was exposed to Ringer's solution (black) and $1 \mu\text{M Ani9}$ (green) and washed in Ringer's solution (gray). (B) I-V relationships measured at the end of the voltage steps from the recordings shown in A. (C) Scatter dot plot with average \pm SEM of the percentage of current inhibition measured at -80 and $+80$ mV ($n = 11$).

by ATP in WT mice at -80 mV (-438 ± 94 pA, $n = 28$) was significantly reduced (-6 ± 10 pA, $n = 16$, Wilcoxon-Mann-Whitney U test) in TMEM16A KO mice (Fig. 8 C).

These results indicate that the transient Ca^{2+} increase elicited by $30 \mu\text{M ATP}$ activates a TMEM16A-dependent current in supporting cells of the olfactory epithelium.

Discussion

Our results provide the first demonstration that supporting cells of the mouse olfactory epithelium have functional Ca^{2+} -activated Cl^- channels that can be activated by purinergic stimulation producing large Cl^- currents. Recordings from TMEM16A KO mice show that TMEM16A is a necessary component of the Ca^{2+} -activated Cl^- currents in olfactory supporting cells.

An important preliminary step to understand the possible physiological roles of TMEM16A in supporting cells is to estimate equilibrium potential for Cl^- (E_{Cl}) to determine the direction of the Cl^- flux. The apical part of supporting cells and their microvilli are immersed in the mucus (Menco and Farbman, 1992; Menco et al., 1998). The concentrations of various ions in the olfactory mucus, dendritic knobs of sensory neurons, and cytosol of supporting cells from rats have been measured by Reuter et al. (1998) using energy-dispersive x-ray microanalysis. They reported that the average concentration of Cl^- was 55 ± 11 mM in the mucus and 32 ± 12 mM in the cytosol of supporting cells (Reuter et al., 1998). Thus, we estimated E_{Cl} at the apical part of supporting cells, where TMEM16A is localized, assuming that (1) the values of Cl^- concentrations in mouse are the same of

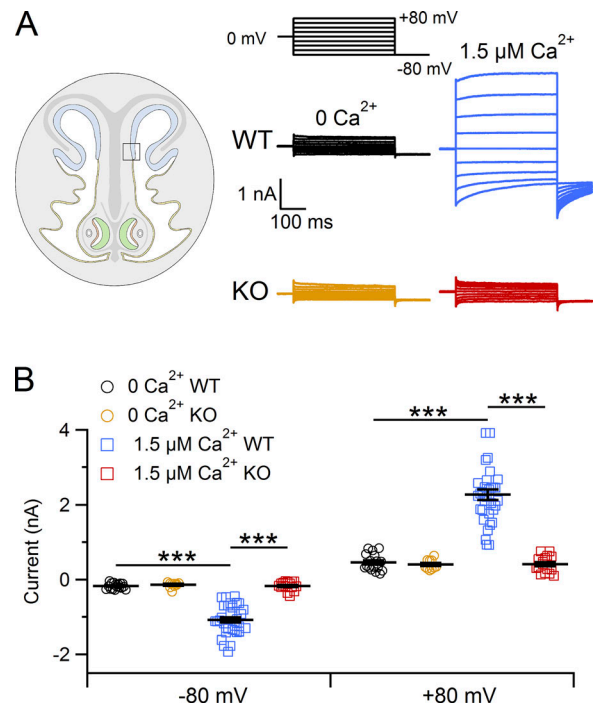


Figure 6. Lack of Ca^{2+} -activated currents in supporting cells from TMEM16A KO mice. (A) Representative whole-cell recordings obtained with pipette solutions containing 0 or $1.5 \mu\text{M Ca}^{2+}$, as indicated. The voltage protocol is reported at the top of the panel. (B) Scatter dot plot with average \pm SEM showing current amplitudes measured at -80 and $+80$ mV in the presence of the following $[\text{Ca}^{2+}]_i$: for WT mice nominally 0 ($n = 17$), $1.5 \mu\text{M}$ ($n = 33$) or for TMEM16A KO mice nominally 0 ($n = 10$), $1.5 \mu\text{M}$ ($n = 16$). ***, $P < 0.001$, Tukey test after one-way ANOVA. Recordings were obtained from supporting cells located close to the transition zone with the respiratory epithelium.

those measured in rats and (2) the Cl^- concentration at the apical part of supporting cells and at the proximal part of their microvilli is the same as that in the cytosol. In these conditions, we obtained a value for E_{Cl} of -14 mV (at room temperature 20 – 25°C). Taking into account that we measured an average value for resting membrane potential of supporting cells of -41 ± 1 mV (that is in agreement with previously measured values in the range between -50 mV and -30 mV; Vogalis et al., 2005a), the calculated electrochemical driving force for Cl^- is -27 mV. Thus, the opening of TMEM16A Cl^- channels by Ca^{2+} at the apical part of supporting cells causes an efflux of Cl^- , contributing to control Cl^- homeostasis and dynamics in the mucus covering the olfactory epithelium.

The mucus composition is fundamental to maintain the ionic environment necessary for olfactory transduction. Indeed, the binding of odorant molecules to odorant receptors in the cilia of olfactory sensory neurons leads to a transduction cascade that includes the activation of CNG channels and the Ca^{2+} -activated Cl^- channels TMEM16B, whose function depends on the Cl^- electrochemical gradient between the mucus and the intraciliary compartment (Pifferi et al., 2009; Stephan et al., 2009; Billig et al., 2011; Pietra et al., 2016; Dibattista et al., 2017; Neureither et al., 2017; Li et al., 2018; Zak et al., 2018; Reisert and Reingruber, 2019). Thus, the Cl^- concentration regulated by

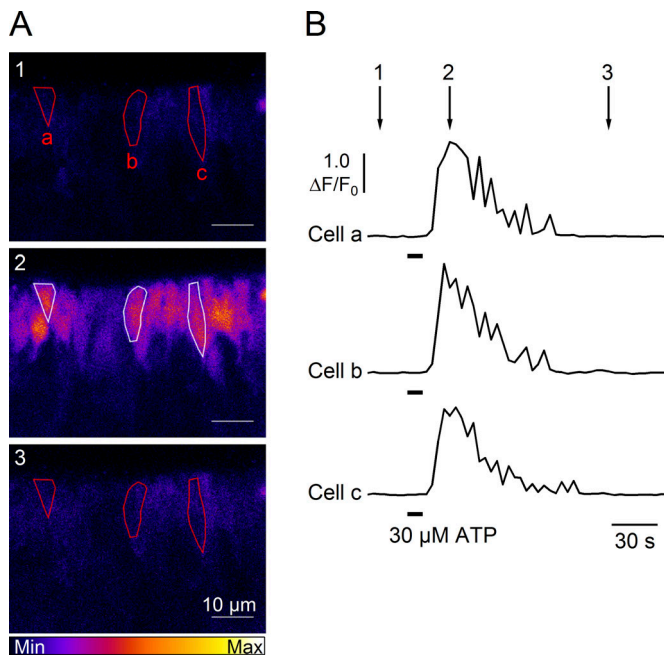


Figure 7. ATP stimulation induces an increase of $[Ca^{2+}]_i$ in supporting cells. (A) Representative sequences of confocal images in pseudocolor from a slice of the olfactory epithelium loaded with Cal520-AM before (1), at the peak (2), and after (3) the response activated by application of 30 μ M ATP for 10 s. (B) Ca^{2+} transients recorded in the cells highlighted in A responding to 30 μ M ATP stimulation. Time points indicated by arrows correspond to frame numbers in A.

TMEM16A would affect the TMEM16B-mediated current, modifying the odorant response of the olfactory sensory neurons.

He et al. (2017) have shown that TMEM16A in epithelial cells is necessary to control the cytoplasmic Cl^- concentration and that an adequate level of Cl^- is necessary for proper endocytic trafficking. In olfactory supporting cells, xenobiotic-metabolizing enzymes are localized in the intracellular compartments, and therefore, the engulfing of xenobiotics is a required step for their detoxification (Ling et al., 2004; Zhuo et al., 2004;

Asakawa et al., 2017). It is of interest to note that some toxic chemicals, such as dichlobenil and methyl iodide, have a more severe noxious effect in the dorsal portion of the olfactory epithelium, where TMEM16A is less expressed (Robinson et al., 2003; Franceschini et al., 2009). Moreover, the endocytosis activity in supporting cells is massively increased by stimulation with acetylcholine via the activation of M3 muscarinic receptors, generating an increase of intracellular Ca^{2+} concentration that could activate the TMEM16A-mediated current (Hegg et al., 2009; Ogura et al., 2011; Fu et al., 2018). The most likely sources of acetylcholine are the microvillous cells, a still poorly understood population of cells that respond to high odorant concentrations and xenobiotic chemicals (Lin et al., 2008; Menini and Pifferi, 2008; Ogura et al., 2011; Fu et al., 2018). In this scenario, the interplay between the acetylcholine response and regulation of Cl^- homeostasis by TMEM16A could regulate the endocytosis and the subsequent xenobiotic detoxification mediated by supporting cells.

Another role of TMEM16A could be the modulation of the purinergic signaling. Supporting cells express metabotropic purinergic P2Y receptors, and extracellular ATP can induce Ca^{2+} release from intracellular stores (Gayle and Burnstock, 2005; Czesnik et al., 2006; Hassenklöver et al., 2008; Hegg et al., 2009). Here, we have shown that ATP produces an intracellular Ca^{2+} increase sufficient to activate the Ca^{2+} -activated Cl^- currents mediated by TMEM16A. Hayoz et al. (2012) reported evidence that ATP is released both through constitutive and evoked release in the olfactory epithelium of neonatal mice. Moreover, the olfactory epithelium receives extensive innervation by various branches of trigeminal nerves (Finger et al., 1990; Schaefer et al., 2002), and these fibers could release ATP through axonal reflex. Interestingly, TMEM16A can amplify the ATP-mediated Ca^{2+} signal by interacting directly with the IP_3R on the ER membrane (Cabrita et al., 2017). Therefore, we can speculate that TMEM16A could be involved in the cascade of the ATP transduction pathway in the olfactory epithelium. In particular, ATP modulates the neuroproliferation partially by the increase of NPY expression in supporting cells (Hassenklöver

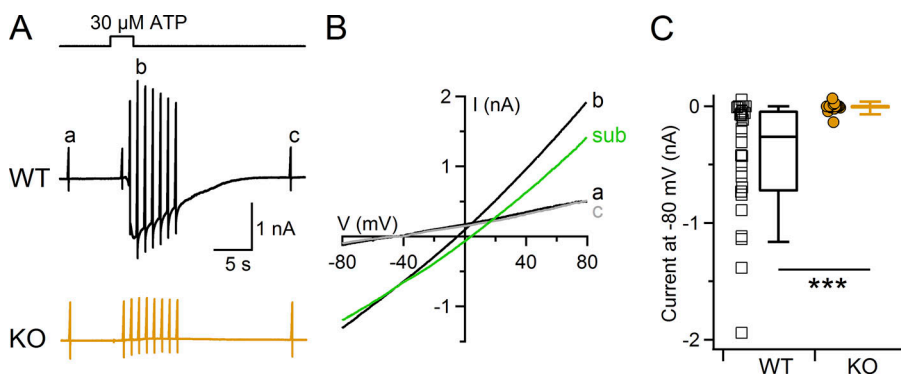


Figure 8. ATP activates a TMEM16A-dependent current in supporting cells. (A) Whole-cell currents activated by 30 μ M ATP from supporting cells located close to the transition zone with the respiratory epithelium from WT (black trace) or TMEM16A KO (orange trace) mice. ATP was applied for the time indicated in the upper trace. The holding potential was -80 mV, and voltage ramps from -80 to $+80$ mV before (a), during (b), and after (c) the ATP response were used to measure the I-V relations. (B) I-V relations from the WT cell shown in A. The green trace (sub) was obtained by subtracting the average between traces a and c from the trace in the presence of ATP (b). (C) Scatter dot plot and box plot showing the peak amplitude of ATP-activated currents measured at -80 mV in WT ($n = 28$) or TMEM16A KO mice ($n = 16$). ***, $P < 0.001$, Wilcoxon-Mann-Whitney U test.

et al., 2008; Jia et al., 2009; Jia and Hegg, 2010). It has been also proposed that ATP could have a neuroprotective function by mediating the expression of HSP25 in supporting cells upon exposure to high odorant concentrations (Hegg and Lucero, 2006).

Conclusions

In summary, our data provide a definitive demonstration that TMEM16A-mediated currents are functional in olfactory supporting cells and provide a foundation for future work investigating the precise physiological role of TMEM16A, possibly using conditional KO mice for TMEM16A, as the constitutive TMEM16A knockout mice used in our study die soon after birth.

Acknowledgments

We thank Anna Boccaccio, Michele Dibattista, and all members of the laboratory for discussions. We also thank Elettra Grdina, Angel Pascual Camerota, Lorenzo Maschietto, and Giovanni Tamburin for mice handling and Helena Krmac and Christina Vlachouli for mice genotyping.

This study was supported by a grant from the Italian Ministry of Education, University, and Research (2010599KBR to A. Menini).

The authors declare no competing financial interests.

Author contributions: T. Henriques and E. Agostinelli performed and analyzed the electrophysiological recordings. A. Hernandez-Clavijo and E. Agostinelli performed and analyzed the Ca²⁺ imaging experiments. D. Kumar Maurya performed and analyzed the immunohistochemistry experiments. J.R. Rock and B.D. Harfe generated and provided the TMEM16A KO mouse model. S. Pifferi contributed to the analysis data. T. Henriques, E. Agostinelli, A. Hernandez-Clavijo, D. Kumar Maurya, S. Pifferi, and A. Menini contributed to the experimental design and manuscript writing. All authors agreed with the final version of the manuscript.

Merritt C. Maduke served as editor.

Submitted: 20 December 2018

Revised: 8 March 2019

Accepted: 15 April 2019

References

Ablimit, A., T. Matsuzaki, Y. Tajika, T. Aoki, H. Hagiwara, and K. Takata. 2006. Immunolocalization of water channel aquaporins in the nasal olfactory mucosa. *Arch. Histol. Cytol.* 69:1-12. <https://doi.org/10.1679/aohc.69.1>

Amjad, A., A. Hernandez-Clavijo, S. Pifferi, D.K. Maurya, A. Boccaccio, J. Franzot, J. Rock, and A. Menini. 2015. Conditional knockout of TMEM16A/anoctamin1 abolishes the calcium-activated chloride current in mouse vomeronasal sensory neurons. *J. Gen. Physiol.* 145: 285-301. <https://doi.org/10.1085/jgp.201411348>

Asakawa, M., Y. Fukutani, A. Savangsuksa, K. Noguchi, H. Matsunami, and M. Yohda. 2017. Modification of the response of olfactory receptors to acetophenone by CYP1a2. *Sci. Rep.* 7:10167. <https://doi.org/10.1038/s41598-017-10862-5>

Barry, P.H. 1994. JPCalc, a software package for calculating liquid junction potential corrections in patch-clamp, intracellular, epithelial and bilayer measurements and for correcting junction potential measurements.

J. Neurosci. Methods. 51:107-116. [https://doi.org/10.1016/0165-0270\(94\)90031-0](https://doi.org/10.1016/0165-0270(94)90031-0)

Benedetto, R., J. Ousingasawat, P. Wanitchakool, Y. Zhang, M.J. Holtzman, M. Amaral, J.R. Rock, R. Schreiber, and K. Kunzelmann. 2017. Epithelial Chloride Transport by CFTR Requires TMEM16A. *Sci. Rep.* 7:12397. <https://doi.org/10.1038/s41598-017-10910-0>

Benedetto, R., I. Cabrita, R. Schreiber, and K. Kunzelmann. 2019. TMEM16A is indispensable for basal mucus secretion in airways and intestine. *FASEB J.* 33:4502-4512. <https://doi.org/10.1096/fj.201801333RRR>

Betto, G., O.L. Cherian, S. Pifferi, V. Cenedese, A. Boccaccio, and A. Menini. 2014. Interactions between permeation and gating in the TMEM16B/anoctamin2 calcium-activated chloride channel. *J. Gen. Physiol.* 143: 703-718. <https://doi.org/10.1085/jgp.201411182>

Billig, G.M., B. Pál, P. Fidzinski, and T.J. Jentsch. 2011. Ca²⁺-activated Cl⁻ currents are dispensable for olfaction. *Nat. Neurosci.* 14:763-769. <https://doi.org/10.1038/nn.2821>

Breipohl, W., H.J. Laugwitz, and N. Bornfeld. 1974. Topological relations between the dendrites of olfactory sensory cells and sustentacular cells in different vertebrates. An ultrastructural study. *J. Anat.* 117:89-94.

Breunig, E., I. Manzini, F. Piscitelli, B. Gutermann, V. Di Marzo, D. Schild, and D. Czesnik. 2010. The endocannabinoid 2-arachidonoyl-glycerol controls odor sensitivity in larvae of *Xenopus laevis*. *J. Neurosci.* 30: 8965-8973. <https://doi.org/10.1523/JNEUROSCI.4030-09.2010>

Cabrita, I., R. Benedetto, A. Fonseca, P. Wanitchakool, L. Sirianant, B.V. Skryabin, L.K. Schenk, H. Pavenstädt, R. Schreiber, and K. Kunzelmann. 2017. Differential effects of anoctamins on intracellular calcium signals. *FASEB J.* 31:2123-2134. <https://doi.org/10.1096/fj.201600797RR>

Cenedese, V., G. Betto, F. Celsi, O.L. Cherian, S. Pifferi, and A. Menini. 2012. The voltage dependence of the TMEM16B/anoctamin2 calcium-activated chloride channel is modified by mutations in the first putative intracellular loop. *J. Gen. Physiol.* 139:285-294. <https://doi.org/10.1085/jgp.201110764>

Chen, Y., M.L. Getchell, X. Ding, and T.V. Getchell. 1992. Immunolocalization of two cytochrome P450 isozymes in rat nasal chemosensory tissue. *Neuroreport.* 3:749-752. <https://doi.org/10.1097/00001756-199209000-00007>

Czesnik, D., J. Kuduz, D. Schild, and I. Manzini. 2006. ATP activates both receptor and sustentacular supporting cells in the olfactory epithelium of *Xenopus laevis* tadpoles. *Eur. J. Neurosci.* 23:119-128. <https://doi.org/10.1111/j.1460-9568.2005.04533.x>

Czesnik, D., D. Schild, J. Kuduz, and I. Manzini. 2007. Cannabinoid action in the olfactory epithelium. *Proc. Natl. Acad. Sci. USA.* 104:2967-2972. <https://doi.org/10.1073/pnas.0609067104>

Dauner, K., J. Lissmann, S. Jeridi, S. Frings, and F. Möhrlein. 2012. Expression patterns of anoctamin 1 and anoctamin 2 chloride channels in the mammalian nose. *Cell Tissue Res.* 347:327-341. <https://doi.org/10.1007/s00441-012-1324-9>

Davidson, J.S., and I.M. Baumgarten. 1988. Glycylrrhethinic acid derivatives: a novel class of inhibitors of gap-junctional intercellular communication. Structure-activity relationships. *J. Pharmacol. Exp. Ther.* 246:1104-1107.

Dibattista, M., A. Mazzatenta, F. Grassi, R. Tirindelli, and A. Menini. 2008. Hyperpolarization-activated cyclic nucleotide-gated channels in mouse vomeronasal sensory neurons. *J. Neurophysiol.* 100:576-586. <https://doi.org/10.1152/jn.90263.2008>

Dibattista, M., S. Pifferi, A. Boccaccio, A. Menini, and J. Reisert. 2017. The long tale of the calcium activated Cl⁻ channels in olfactory transduction. *Channels (Austin)*. 11:399-414. <https://doi.org/10.1080/19336950.2017.1307489>

Finger, T.E., V.L. St Jeor, J.C. Kinnamon, and W.L. Silver. 1990. Ultrastructure of substance P- and CGRP-immunoreactive nerve fibers in the nasal epithelium of rodents. *J. Comp. Neurol.* 294:293-305. <https://doi.org/10.1002/cne.902940212>

Franceschini, V., S. Bettini, S. Pifferi, A. Rosellini, A. Menini, R. Saccardi, E. Ognio, R. Jeffery, R. Poulson, and R.P. Revoltella. 2009. Human cord blood CD133+ stem cells transplanted to nod-scid mice provide conditions for regeneration of olfactory neuroepithelium after permanent damage induced by dichlobenil. *Stem Cells.* 27:825-835. <https://doi.org/10.1002/stem.11>

Fu, Z., T. Ogura, W. Luo, and W. Lin. 2018. ATP and Odor Mixture Activate TRPM5-Expressing Microvillous Cells and Potentially Induce Acetylcholine Release to Enhance Supporting Cell Endocytosis in Mouse Main Olfactory Epithelium. *Front. Cell. Neurosci.* 12:71. <https://doi.org/10.3389/fncel.2018.00071>

Gayle, S., and G. Burnstock. 2005. Immunolocalisation of P2X and P2Y nucleotide receptors in the rat nasal mucosa. *Cell Tissue Res.* 319:27-36. <https://doi.org/10.1007/s00441-004-0979-2>

- Grubb, B.R., T.D. Rogers, H.M. Kulaga, K.A. Burns, R.L. Wonsetler, R.R. Reed, and L.E. Ostrowski. 2007. Olfactory epithelia exhibit progressive functional and morphological defects in CF mice. *Am. J. Physiol. Cell Physiol.* 293:C574–C583. <https://doi.org/10.1152/ajpcell.00106.2007>
- Gu, J., Q.Y. Zhang, M.B. Genter, T.W. Lipinskas, M. Negishi, D.W. Nebert, and X. Ding. 1998. Purification and characterization of heterologously expressed mouse CYP2A5 and CYP2G1: role in metabolic activation of acetaminophen and 2,6-dichlorobenzonitrile in mouse olfactory mucosal microsomes. *J. Pharmacol. Exp. Ther.* 285:1287–1295.
- Hassenklöver, T., S. Kurtanska, I. Bartoszek, S. Junek, D. Schild, and I. Manzini. 2008. Nucleotide-induced Ca²⁺ signaling in sustentacular supporting cells of the olfactory epithelium. *Glia.* 56:1614–1624. <https://doi.org/10.1002/glia.20714>
- Hassenklöver, T., P. Schwartz, D. Schild, and I. Manzini. 2009. Purinergic signaling regulates cell proliferation of olfactory epithelium progenitors. *Stem Cells.* 27:2022–2031. <https://doi.org/10.1002/stem.126>
- Hayoz, S., C. Jia, and C. Hegg. 2012. Mechanisms of constitutive and ATP-evoked ATP release in neonatal mouse olfactory epithelium. *BMC Neurosci.* 13:53. <https://doi.org/10.1186/1471-2202-13-53>
- He, M., W. Ye, W.-J. Wang, E.S. Sison, Y.N. Jan, and L.Y. Jan. 2017. Cytoplasmic Cl⁻ couples membrane remodeling to epithelial morphogenesis. *Proc. Natl. Acad. Sci. USA.* 114:E11161–E11169. <https://doi.org/10.1073/pnas.1714448115>
- Hegg, C.C., and M.T. Lucero. 2006. Purinergic receptor antagonists inhibit odorant-induced heat shock protein 25 induction in mouse olfactory epithelium. *Glia.* 53:182–190. <https://doi.org/10.1002/glia.20258>
- Hegg, C.C., D. Greenwood, W. Huang, P. Han, and M.T. Lucero. 2003. Activation of purinergic receptor subtypes modulates odor sensitivity. *J. Neurosci.* 23:8291–8301. <https://doi.org/10.1523/JNEUROSCI.23-23-08291.2003>
- Hegg, C.C., M. Irwin, and M.T. Lucero. 2009. Calcium store-mediated signaling in sustentacular cells of the mouse olfactory epithelium. *Glia.* 57:634–644. <https://doi.org/10.1002/glia.20792>
- Huang, F., X. Wong, and L.Y. Jan. 2012. International Union of Basic and Clinical Pharmacology. LXXXV: calcium-activated chloride channels. *Pharmacol. Rev.* 64:1–15. <https://doi.org/10.1124/pr.111.005009>
- Jia, C., and C.C. Hegg. 2010. NPY mediates ATP-induced neuroproliferation in adult mouse olfactory epithelium. *Neurobiol. Dis.* 38:405–413. <https://doi.org/10.1016/j.nbd.2010.02.013>
- Jia, C., J.P. Doherty, S. Crudgington, and C.C. Hegg. 2009. Activation of purinergic receptors induces proliferation and neuronal differentiation in Swiss Webster mouse olfactory epithelium. *Neuroscience.* 163:120–128. <https://doi.org/10.1016/j.neuroscience.2009.06.040>
- Jia, C., C. Roman, and C.C. Hegg. 2010. Nickel sulfate induces location-dependent atrophy of mouse olfactory epithelium: protective and proliferative role of purinergic receptor activation. *Toxicol. Sci.* 115:547–556. <https://doi.org/10.1093/toxsci/kfq071>
- Keller, A., and F.L. Margolis. 1975. Immunological studies of the rat olfactory marker protein. *J. Neurochem.* 24:1101–1106. <https://doi.org/10.1111/j.1471-4159.1975.tb03883.x>
- Kunzelmann, K., I. Cabrita, P. Wanitchakool, J. Ousingsawat, L. Sirianant, R. Benedetto, and R. Schreiber. 2016. Modulating Ca²⁺ signals: a common theme for TMEM16, Ist2, and TMC. *Pflugers Arch.* 468:475–490. <https://doi.org/10.1007/s00424-015-1767-4>
- Lacroix, M.-C., K. Badonnel, N. Meunier, F. Tan, C. Schlegel-Le Poupon, D. Durieux, R. Monnerie, C. Baly, P. Congar, R. Saless, and M. Caillol. 2008. Expression of insulin system in the olfactory epithelium: first approaches to its role and regulation. *J. Neuroendocrinol.* 20:1176–1190. <https://doi.org/10.1111/j.1365-2826.2008.01777.x>
- Li, R.-C., C.-C. Lin, X. Ren, J.S. Wu, L.L. Molday, R.S. Molday, and K.-W. Yau. 2018. Ca²⁺-activated Cl current predominates in threshold response of mouse olfactory receptor neurons. *Proc. Natl. Acad. Sci. USA.* 115:5570–5575. <https://doi.org/10.1073/pnas.1803443115>
- Lin, W., T. Ogura, R.F. Margolskee, T.E. Finger, and D. Restrepo. 2008. TRPM5-expressing solitary chemosensory cells respond to odorous irritants. *J. Neurophysiol.* 99:1451–1460. <https://doi.org/10.1152/jn.01195.2007>
- Ling, G., J. Gu, M.B. Genter, X. Zhuo, and X. Ding. 2004. Regulation of cytochrome P450 gene expression in the olfactory mucosa. *Chem. Biol. Interact.* 147:247–258. <https://doi.org/10.1016/j.cbi.2004.02.003>
- Lu, D.C., H. Zhang, Z. Zador, and A.S. Verkman. 2008. Impaired olfaction in mice lacking aquaporin-4 water channels. *FASEB J.* 22:3216–3223. <https://doi.org/10.1096/fj.07-104836>
- Maurya, D.K., and A. Menini. 2014. Developmental expression of the calcium-activated chloride channels TMEM16A and TMEM16B in the mouse olfactory epithelium. *Dev. Neurobiol.* 74:657–675. <https://doi.org/10.1002/dneu.22159>
- Maurya, D.K., T. Henriques, M. Marini, N. Pedemonte, L.J.V. Galiotta, J.R. Rock, B.D. Harfe, and A. Menini. 2015. Development of the Olfactory Epithelium and Nasal Glands in TMEM16A^{-/-} and TMEM16A^{+/+} Mice. *PLoS One.* 10:e0129171. <https://doi.org/10.1371/journal.pone.0129171>
- Menco, B.P., and A.I. Farbman. 1992. Ultrastructural evidence for multiple mucous domains in frog olfactory epithelium. *Cell Tissue Res.* 270:47–56. <https://doi.org/10.1007/BF00381878>
- Menco, B.P., G.B. Birrell, C.M. Fuller, P.I. Ezeh, D.A. Keeton, and D.J. Benos. 1998. Ultrastructural localization of amiloride-sensitive sodium channels and Na⁺/K⁺-ATPase in the rat's olfactory epithelial surface. *Chem. Senses.* 23:137–149. <https://doi.org/10.1093/chemse/23.2.137>
- Menini, A., and S. Pifferi. 2008. New whiffs about chemesthesis. Focus on “TRPM5-expressing solitary chemosensory cells respond to odorous irritants”. *J. Neurophysiol.* 99:1055–1056. <https://doi.org/10.1152/jn.00043.2008>
- Merigo, F., C. Mucignat-Caretta, M. Cristofolletti, and C. Zancanaro. 2011. Epithelial membrane transporters expression in the developing to adult mouse vomeronasal organ and olfactory mucosa. *Dev. Neurobiol.* 71:854–869. <https://doi.org/10.1002/dneu.20944>
- Neureither, F., N. Stowasser, S. Frings, and F. Möhrlein. 2017. Tracking of unfamiliar odors is facilitated by signal amplification through anoctamin-2 chloride channels in mouse olfactory receptor neurons. *Physiol. Rep.* 5:e13373. <https://doi.org/10.14814/phy2.13373>
- Ogura, T., S.A. Szebenyi, K. Krosnowski, A. Sathyanesan, J. Jackson, and W. Lin. 2011. Cholinergic microvillous cells in the mouse main olfactory epithelium and effect of acetylcholine on olfactory sensory neurons and supporting cells. *J. Neurophysiol.* 106:1274–1287. <https://doi.org/10.1152/jn.00186.2011>
- Patton, C., S. Thompson, and D. Epel. 2004. Some precautions in using chelators to buffer metals in biological solutions. *Cell Calcium.* 35:427–431. <https://doi.org/10.1016/j.ceca.2003.10.006>
- Pedemonte, N., and L.J.V. Galiotta. 2014. Structure and function of TMEM16 proteins (anoctamins). *Physiol. Rev.* 94:419–459. <https://doi.org/10.1152/physrev.00039.2011>
- Pfister, S., T. Weber, W. Härtig, C. Schwerdel, R. Elsaesser, I. Knuesel, and J.-M. Fritschy. 2015. Novel role of cystic fibrosis transmembrane conductance regulator in maintaining adult mouse olfactory neuronal homeostasis. *J. Comp. Neurol.* 523:406–430. <https://doi.org/10.1002/cne.23686>
- Pietra, G., M. Dibattista, A. Menini, J. Reisert, and A. Boccaccio. 2016. The Ca²⁺-activated Cl⁻ channel TMEM16B regulates action potential firing and axonal targeting in olfactory sensory neurons. *J. Gen. Physiol.* 148:293–311. <https://doi.org/10.1085/jgp.201611622>
- Pifferi, S., G. Pascarella, A. Boccaccio, A. Mazzatenta, S. Gustincich, A. Menini, and S. Zucchelli. 2006. Bestrophin-2 is a candidate calcium-activated chloride channel involved in olfactory transduction. *Proc. Natl. Acad. Sci. USA.* 103:12929–12934. <https://doi.org/10.1073/pnas.0604505103>
- Pifferi, S., M. Dibattista, and A. Menini. 2009. TMEM16B induces chloride currents activated by calcium in mammalian cells. *Pflugers Arch.* 458:1023–1038. <https://doi.org/10.1007/s00424-009-0684-9>
- Piperno, G., and M.T. Fuller. 1985. Monoclonal antibodies specific for an acetylated form of alpha-tubulin recognize the antigen in cilia and flagella from a variety of organisms. *J. Cell Biol.* 101:2085–2094. <https://doi.org/10.1083/jcb.101.6.2085>
- Rash, J.E., K.G.V. Davidson, N. Kamasawa, T. Yasumura, M. Kamasawa, C. Zhang, R. Michaels, D. Restrepo, O.P. Ottersen, C.O. Olson, and J.I. Nagy. 2005. Ultrastructural localization of connexins (Cx36, Cx43, Cx45), glutamate receptors and aquaporin-4 in rodent olfactory mucosa, olfactory nerve and olfactory bulb. *J. Neurocytol.* 34:307–341. <https://doi.org/10.1007/s11068-005-8360-2>
- Reisert, J., and J. Reingruber. 2019. Ca²⁺-activated Cl⁻ current ensures robust and reliable signal amplification in vertebrate olfactory receptor neurons. *Proc. Natl. Acad. Sci. USA.* 116:1053–1058. <https://doi.org/10.1073/pnas.1816371116>
- Reuter, D., K. Zierold, W.H. Schröder, and S. Frings. 1998. A depolarizing chloride current contributes to chemoelectrical transduction in olfactory sensory neurons in situ. *J. Neurosci.* 18:6623–6630. <https://doi.org/10.1523/JNEUROSCI.18-17-06623.1998>
- Robinson, D.A., J.R. Foster, J.A. Nash, and C.J. Reed. 2003. Three-dimensional mapping of the lesions induced by beta-beta'-iminodipropionitrile, methyl iodide and methyl methacrylate in the rat nasal cavity. *Toxicol. Pathol.* 31:340–347. <https://doi.org/10.1080/01926230390204388>

- Rochelle, L.G., D.C. Li, H. Ye, E. Lee, C.R. Talbot, and R.C. Boucher. 2000. Distribution of ion transport mRNAs throughout murine nose and lung. *Am. J. Physiol. Lung Cell. Mol. Physiol.* 279:L14-L24. <https://doi.org/10.1152/ajplung.2000.279.1.L14>
- Rock, J.R., C.R. Futtner, and B.D. Harfe. 2008. The transmembrane protein TMEM16A is required for normal development of the murine trachea. *Dev. Biol.* 321:141-149. <https://doi.org/10.1016/j.ydbio.2008.06.009>
- Rock, J.R., W.K. O'Neal, S.E. Gabriel, S.H. Randell, B.D. Harfe, R.C. Boucher, and B.R. Grubb. 2009. Transmembrane protein 16A (TMEM16A) is a Ca²⁺-regulated Cl⁻ secretory channel in mouse airways. *J. Biol. Chem.* 284:14875-14880. <https://doi.org/10.1074/jbc.C109.000869>
- Schaefer, M.L., B. Böttger, W.L. Silver, and T.E. Finger. 2002. Trigeminal collaterals in the nasal epithelium and olfactory bulb: a potential route for direct modulation of olfactory information by trigeminal stimuli. *J. Comp. Neurol.* 444:221-226. <https://doi.org/10.1002/cne.10143>
- Seo, Y., H.K. Lee, J. Park, D.-K. Jeon, S. Jo, M. Jo, and W. Namkung. 2016. Ani9, A Novel Potent Small-Molecule ANO1 Inhibitor with Negligible Effect on ANO2. *PLoS One.* 11:e0155771. <https://doi.org/10.1371/journal.pone.0155771>
- Shimazaki, R., A. Boccaccio, A. Mazzatenta, G. Pinato, M. Migliore, and A. Menini. 2006. Electrophysiological properties and modeling of murine vomeronasal sensory neurons in acute slice preparations. *Chem. Senses.* 31:425-435. <https://doi.org/10.1093/chemse/bjj047>
- Stephan, A.B., E.Y. Shum, S. Hirsh, K.D. Cygnar, J. Reisert, and H. Zhao. 2009. ANO2 is the ciliary calcium-activated chloride channel that may mediate olfactory amplification. *Proc. Natl. Acad. Sci. USA.* 106:11776-11781. <https://doi.org/10.1073/pnas.0903304106>
- Suzuki, Y., M. Takeda, and A.I. Farbman. 1996. Supporting cells as phagocytes in the olfactory epithelium after bulbectomy. *J. Comp. Neurol.* 376: 509-517. [https://doi.org/10.1002/\(SICI\)1096-9861\(19961223\)376:4<509::AID-CNEI>3.0.CO;2-5](https://doi.org/10.1002/(SICI)1096-9861(19961223)376:4<509::AID-CNEI>3.0.CO;2-5)
- Thomas, D., S.C. Tovey, T.J. Collins, M.D. Bootman, M.J. Berridge, and P. Lipp. 2000. A comparison of fluorescent Ca²⁺ indicator properties and their use in measuring elementary and global Ca²⁺ signals. *Cell Calcium.* 28: 213-223. <https://doi.org/10.1054/ceca.2000.0152>
- Vogalis, F., C.C. Hegg, and M.T. Lucero. 2005a. Ionic conductances in sustentacular cells of the mouse olfactory epithelium. *J. Physiol.* 562: 785-799. <https://doi.org/10.1113/jphysiol.2004.079228>
- Vogalis, F., C.C. Hegg, and M.T. Lucero. 2005b. Electrical coupling in sustentacular cells of the mouse olfactory epithelium. *J. Neurophysiol.* 94: 1001-1012. <https://doi.org/10.1152/jn.01299.2004>
- Whitby-Logan, G.K., M. Weech, and E. Walters. 2004. Zonal expression and activity of glutathione S-transferase enzymes in the mouse olfactory mucosa. *Brain Res.* 995:151-157. <https://doi.org/10.1016/j.brainres.2003.09.012>
- Wong, W.M., M. Nagel, A. Hernandez-Clavijo, S. Pifferi, A. Menini, M. Spehr, and J.P. Meeks. 2018. Sensory Adaptation to Chemical Cues by Vomeronasal Sensory Neurons. *eNeuro.* 5:ENEURO.0223-18.2018. <https://doi.org/10.1523/ENEURO.0223-18.2018>
- Zak, J.D., J. Grimaud, R.-C. Li, C.-C. Lin, and V.N. Murthy. 2018. Calcium-activated chloride channels clamp odor-evoked spike activity in olfactory receptor neurons. *Sci. Rep.* 8:10600. <https://doi.org/10.1038/s41598-018-28855-3>
- Zhuo, X., J. Gu, M.J. Behr, P.J. Swiatek, H. Cui, Q.-Y. Zhang, Y. Xie, D.N. Collins, and X. Ding. 2004. Targeted disruption of the olfactory mucosa-specific Cyp2g1 gene: impact on acetaminophen toxicity in the lateral nasal gland, and tissue-selective effects on Cyp2a5 expression. *J. Pharmacol. Exp. Ther.* 308:719-728. <https://doi.org/10.1124/jpet.103.060301>